An energy time-convexity second-order synchrosqueezing transform and application in weak fault diagnosis of rolling bearings in an aerospace engine

OPEN ACCESS
IOP Publishing
Measurement Science and Technology
Meas. Sci. Technol. **31** (2020) 125105 (19pp)
https://doi.org/10.1088/1361-6501/ab983f

An energy time-convexity second-order synchrosqueezing transform and application in weak fault diagnosis of rolling bearings in an aerospace engine

Zhenyi Chen[1], Yanyang Zi[1], Ping Li[2], Jinglong Chen[1] and Kaifu Xu[2]

[1] School of Mechanical Engineering, State Key Laboratory for Manufacturing and Systems Engineering, Xi'an Jiaotong University, Xi'an 710049, People's Republic of China
[2] Xi'an Aerospace Propulsion Institution, Xi'an 710100, People's Republic of China

E-mail: ziyy@mail.xjtu.edu.cn

Received 25 February 2020, revised 23 May 2020
Accepted for publication 1 June 2020
Published 9 October 2020

Abstract

Although the original short-time Fourier-transform-based synchrosqueezing transform (FSST) and its second-order transform (FSST2) can effectively improve the readability of quasi-stationary signal and time-varying signal, respectively, the weak components of time–frequency representation are often submerged easily by noises and large-amplitude instantaneous frequencies (IFs). Moreover, aerospace engines always work in fierce vibration and non-steady states, and this easily causes the weak fault feature of rolling bearings obscured in the time–frequency domain. To solve this problem, we propose a time–frequency analysis algorithm called energy time-convexity second-order synchrosqueezing transform (ET-FSST2). This can sharpen the time-varying IFs like FSST2, and more importantly, it can extract the time-varying IFs with small amplitudes such as weak impulse-like components from multi-component vibration signals. The ET-FSST2 firstly calculates the energy convexity function in the time direction to extract the non-stationary IFs after employing FSST2. It then structures an optimization function by combining a hyperbolic tangent function with a chi-square distribution function as well as optimizing the targeted parameters, aiming to extract the weak components of the non-stationary IFs. Moreover, the effectiveness and robustness of the proposed method are validated by numerical simulation and rolling bearing fault tests. Finally, two case studies of weak fault diagnosis of Ni–Cu–Ag-based PVD-coated rolling bearings operating in cryogenic surroundings are given to illustrate the effectiveness of the proposed method for aerospace engine bearing fault diagnosis.

Keywords: aerospace engine, fault diagnosis, synchrosqueezing transform, time–frequency analysis, cryogenic environment

(Some figures may appear in colour only in the online journal)

1. Introduction

As advanced aerospace engines commonly have sophisticated systems and structures, the phenomena of aerospace engine misdiagnosis and missed diagnosis are especially serious, so it necessitates the development of reliable vibration monitoring and fault diagnosis technologies [1, 2]. To date, several studies have shown that many conventional properties and

mechanisms at cryogenic temperature are no longer applicable compared to those in normal temperature, such as performance of materials, behaviors of tribology [3, 4], lubrication [5] and wear [6], which easily cause the fatigue and damage of aerospace engine components such as rolling bearings serviced in a cryogenic environment. In addition, the working processes of aerospace engines often cause complex and fierce vibration [7, 8], and the vibration signals always contain time-varying multi-components with different amplitudes resulting from the multi-source vibration such as unsteady combustion, fluid excitation, vibration of the turbopump, etc [9, 10], making the vibration analysis a challenging task. Moreover, the weak faults of rolling bearings often result in small-amplitude impulse-like components which are easily submerged in the vibration signals [11, 12], especially when the vibration signals are collected from the out-shell of the turbopump [1, 13], and this further increases the difficulty of its fault diagnosis. Hence, it is significant to explore advanced and suitable methods for the health monitoring and fault diagnosis of the rolling bearings in aerospace engines based on vibration signals [2, 14]. Similar requirements are also common in large rotating machines such as aeroengines [15], gas turbine engines [16] etc.

The time–frequency analysis (TFA) method is a common and effective vibration signal analysis method for mechanical fault diagnosis, because the instantaneous frequency (IF) can be clearly characterized on the time–frequency plane [17, 18]. Accordingly, lots of TFA methods such as the Wigner–Ville distribution (WVD) [19], short-time Fourier transform (STFT), wavelet transform (WT) [20] and S-transform have been applied in mechanical condition monitoring and fault diagnosis [21]. However, the aforementioned original time–frequency representations (TFR) have their own limitation [22, 23]. For instance, the WVD is restricted by the presence of cross-terms which is a serious limitation for non-stationary signals [24], while the STFT and WT are restricted owing to the Heisenberg uncertainty principle [25]. The frequency-dependent window function adopted by ST would easily lead to an insufficient time resolution at the low-frequency stage and a non-ideal frequency resolution in the high-frequency band [26, 27]. In addition, none of the abovementioned methods have enough energy concentration. Hence in order to sharpen the ridgeline to improve the readability of TFR for vibration signals, plenty of algorithms have been explored. Daubechies proposed the synchrosqueezing transform (SST) which can determine the time–frequency components of a time-dependent signal containing multiple oscillatory modes [28, 29]. It can not only reconstruct the signal to the time domain, but also improve the readability of TFR of signals with slowly varying IFs [30].

However, the applicability of SST is somewhat limited by the requirements of fast-varying frequency for the modes constituting the signal, and the IFs are blurred in both time and scale/frequency directions [31, 32]. Lately, many ameliorated methods based on SST have been proposed to sharpen the TFR of a non-stationary signal. Jiang and Suter introduced an instantaneous frequency-embedded synchrosqueezing wavelet transform (IFE-SST) for a rough estimation of the IF of a targeted component to produce accurate IF estimation [33]. Yu and Lin explored an time-reassigned multisynchrosqueezing transform (TMSST) to extract fast frequency-varying signal such as impulse components from the signal, and this method is also effective for signal reconstructions [34]. Wang and Chen studied a matching demodulation transform (MDT), which does not necessitate a special parametric TF dictionary, and it could reduce the obscurity of the curved IFs [35]. Yu and Ma embedded the second-order two-dimensional IF estimation into the multisynchrosqueezing transform, and this algorithm improved the high time–frequency resolution [36]. Qu and Chen explored a synchrosqueezed adaptive wavelet transform (SSAWT) to analyze the arbitrary time series, and the center frequencies and scaling factors were optimized [37]. Behera and Meignen proposed the second-order synchrosqueezing transform (SST2): one of the generalized theoretical methods of TFA based on SST, with the aim of coping with a strong FM signal by computing a second-order local approximation of the IF [38]. Moreover, it was proved to be effective for a linear chirps signal [36].

Especially, in the field of rotating machinary monitoring and fault diagnosis, Wang and Chen proposed a matching synchrosqueezing transform (MSST), which incorporated the IF estimation and the group delay estimation to change the chirp rate estimation into a comprehensive and accurate IF estimation, and applied it in aeroengine monitoring [39]. Yu and Lin combined the polynomial chirplet transform and synchroextracting algorithm to analyze nonstationary and multi-component features from the vibration signals, which was further adopted in the IF extraction for the signal of rotating machinery [25]. Chen and Zuo proposed an ameliorated synchroextracting transform (ASET) which employed the second-order Talor expansion to analyze fast time-varying and strong frequency-modulated signal for vibration analysis of a rotating machine [40]. Cao proposed a time-reassigned synchrosqueezing transform to sharpen the IF in the time direction which was applied to analyze the impulse-like signal caused by a compressor defect [31]. Yu explored a concentrated TFA method that could characterize the transient components from the vibration signal, as well as improve the sharpness of the IFs. It was then applied in rolling bearing fault detection [24]. Even so, the scalogram in the time–frequency domain consists of lines that represent their own amplitudes. As for the small-amplitude fast-varying IFs such as weak impulse-like signals, the amplitudes of which are much smaller than other IFs on the *t–f* plane, the ridge lines will be easily blurred, and this further restricts the state monitoring and weak fault identification of the rotating machinery.

In this case, a method to extract small-amplitude time-varying IFs and improve their readability of the TFR from the raw signals to overcome the unintelligibility has been a challenge. Here we propose an energy time-convexity second-order synchrosqueezing transform (ET-FSST2), which retains the advantage of FSST2 for sharpening fast-varying IFs. The essence of the ET-FSST2 contains three points as follows. Firstly, the convexity function in the time direction is calculated to extract the fast-varying IFs from the non-stationary signal after employing the FSST2. Secondly, an

optimization function is structured by combining a hyperbolic tangent function with a chi-square distribution function in addition to optimizing its parameters. Finally, by multiplying the above two functions, the small-amplitude time-varying IFs are extracted from the signal in the time–frequency domain.

In practice, the vibration signals of the aerospace engine contain multi-components with different amplitudes, and the vibrations resulting from rolling bearing faults are relatively weak. Even though the conventional TFA methods such as FSST and FSST2 are employed, the IFs of fault characteristics are still blurred, thus we explore the application of ET-FSST2 in aerospace engine fault diagnosis. The main advantage of the ET-FSST2 is that it can effectively retain the property of FSST2 in TFR sharpness of non-stationary vibration signals, and more importantly, the adjustive weak characteristic extraction property enables diagnosis of weak faults such as rolling bearing faults and other mechanical component defects in aerospace engines.

The paper is organized as follows: section 2 introduces the theoretical basis of FSST and FSST2, section 3 describes the proposed method (ET-FSST2), section 4 shows the simulation to validate its effectiveness and robustness, and subsequently section 5 gives three case studies in the cryogenic exfoliation diagnosis of the rolling bearings in an aerospace engine. Finally, section 6 presents the conclusion.

2. Theoretical basis

2.1. STFT-based synchrosqueezing transform (FSST)

Suppose $x(t)$ is a purely harmonic signal such that $x(t) = A(t)\,\mathrm{e}^{2i\pi\phi(t)}$, the relative IF is f_0 and the amplitude is constant A_0. For a given window function $g(u)$, the STFT of signal $x(t)$ is defined as

$$S_x^g(u,\xi) = \int_0^{+\infty} x(t)\,g(u-t)\,\mathrm{e}^{-\mathrm{i}2\pi(t-u)}\mathrm{d}t. \tag{1}$$

The STFT is given as follows according to Plancherel's theorem:

$$S_x^g(u,\xi) = \frac{1}{2\pi}\int_{-\infty}^{+\infty} X(\omega)\hat{g}(\omega-\xi)\,\mathrm{e}^{-i\omega u}d\omega = A\hat{g}(2\pi f_0-\xi)\,\mathrm{e}^{i}. \tag{2}$$

In addition, the time-shift derivative of the signal's TF representation $S_x^g(u,\xi)$ is given by

$$\partial_u S_x^g(u,\xi) = i2\pi f_0 \cdot S_x^g(u,\xi) \tag{3}$$

Then, a candidate instantaneous frequency $\omega_s(a,b)$ for the signal $s(t)$ at any $(a,\ b)$ satisfying $S_x^g(u,\xi)\neq 0$ can be calculated as

$$f_0(u,\xi)\,\{\ \begin{matrix}\left|\frac{\partial_u S_x^g(u,\xi)}{2\pi\cdot S_x^g(u,\xi)}\right|, S_x^g(u,\xi) > \lambda \\ \infty,\ S_x^g(u,\xi) \le \lambda\end{matrix} \tag{4}$$

where λ is the hard threshold on $S_x^g(u,\xi)$, which is applied to overcome the shortcoming that $|S_x^g(u,\xi)|\approx 0$ is rather unstable when signals have been contaminated by noise. The reassignment calculation can be performed according to the map (u,ξ) to $(u, f_0(u,\xi))$ after the IF$(f_0(u,\xi))$is obtained, and the SST is energy reassignment by summing different contributions as

$$T_s^{g,\gamma}(u,\xi) = \frac{1}{g^*(0)}\int_{\left\{\xi, S_x^g(u,\xi)\le\lambda\right\}} S_x^g(u,\xi)\,\delta(\omega-\omega_x(u,\xi))\,d\xi \tag{5}$$

where δ denotes the Dirac distribution.

In addition, the dispersed form of FSST is written as

$$T_s^{g,\gamma}(u,\xi) = \frac{1}{g^*(0)}\sum_{\xi_k:|f_0(u,\xi_k)|\le\Delta f/2} S_x^g(u,\xi)\,\Delta\xi \tag{6}$$

where ξ_k is the discrete value of the scale ξ for applications and $\xi_k-\xi_{k-1}=(\Delta\xi)_k$, and the synchrosqueezing is determined only at the frequency centers ξ_l of the interval $[\xi_l-(1/2)\,\Delta\xi, \xi_l+(1/2)\,\Delta\xi]$, and $\Delta\xi=\xi_l-\xi_{l-1}$.

FSST, belonging to a member of the TFR family, is an extension of the STFT for energy concentration. However, it is proved that $T_s^{g,r}(u,\xi)$ is concentrated in a narrow band around the lines of IF on the *t–f* plane. To solve its limitation, FSST2 was proposed as follows.

2.2. Second-order STFT-based synchrosqueezing transform (FSST2)

An algorithm based on FSST was proposed on a more accurate form of IF extraction, which is defined as the second-order synchrosqueezing transform (FSST2). FSST2 has several propositions. Here we give one of the common definitions to explain the essence as follows:

Proposition: Let a signal $x\in L^2(R)$; the complex reassignment calculation $\varpi(u,\xi)$ and $\tilde{\tau}(u,\xi)$ are defined as follows if $S_x^g(u,\xi)\neq 0$ and

$$\begin{cases}\varpi(u,\xi) = \dfrac{\partial_u S_x^g(u,\xi)}{2i\pi S_x^g(u,\xi)} \\ \tilde{\tau}(u,\xi) = u - \dfrac{\partial_\xi S_x^g(u,\xi)}{2i\pi S_x^g(u,\xi)}.\end{cases} \tag{7}$$

The next step is to calculate the second-order local complex modulation operator for which $\partial_u\tilde{\tau}(u,\xi)\neq 0$:

$$\tilde{q}_x(u,\xi) = \frac{\partial_u\varpi(u,\xi)}{\partial_u\tilde{\tau}\ (u,\xi)}. \tag{8}$$

After the reassignment vector $\tilde{q}_x(u,\xi)$ is obtained, the following discussion shows how the precise frequency modulation is estimated.

Definition: Supposing a signal $x\in L^2(R)$, the second local IF is estimated as

$$\tilde{\omega}\ (u,\xi) = \begin{cases}\varpi(u,\xi)+\tilde{q}_x(u,\xi)\,(u-\tilde{\tau}\ (u,\xi)), \tilde{\tau}\ (u,\xi)\neq 0 \\ \varpi(u,\xi),\ \text{otherwise.}\end{cases} \tag{9}$$

Then, the real part of $\tilde{\omega}\ (u,\xi)$ is the estimate of IF as

$$\tilde{\omega}_r\ (u,\xi) = \mathrm{Re}\left[\tilde{\omega}\ (u,\xi)\right]. \tag{10}$$

After the calculation above, FSST2 is obtained after replacing $\varpi(u,\xi)$by $\tilde{\omega}_r\ (u,\xi)$ in the following form:

$$T_{2,s}^{g,\gamma}(u,\xi)=\frac{1}{g^*(0)}\int_{\left\{\xi,S_x^g(u,\xi)\le\lambda\right\}}S_x^g(u,\xi)\,\delta\left(\omega-\tilde{\omega}_r\ (u,\xi)\right)d\xi. \tag{11}$$

The above analysis shows the essence of FSST2, and the theoretical explanation is detailed in [38].

As mentioned above, the small-amplitude fast-varying IFs to be analyzed on the *t–f* plane will be easily submerged by large-amplitude IFs even though FSST2 is applied, which limits the weak feature extraction. Hence, a TFA method for small-amplitude fast-varying IF extraction based on FSST2 is proposed, and it will be discussed in the following section.

3. Energy time-convexity of second-order STFT-based synchrosqueezing transform

In this section, we provide the rationale of the proposed method named ET-FSST2: a novel TFR method by improving the second-order STFT-based synchrosqueezing transform, by which the small-amplitude fast-varing IFs can be extracted from the multi-component signal in the time–frequency domain, and then present the process of its parameter optimization and the method of its performance measurement.

3.1. Rationale of the proposed method

Based on FSST2, the square of FSST2 is calculated as follows:

$$E_{\mathrm{w}}(u,\xi)=\left[T_{2,f}^{g,r}(u,\xi_k)\right]^2 \tag{12}$$

In practice, the energy spectrum prevails over the frequency spectrum in extracting the targeted features of vibration signals [41, 42]. However, when the signals have low signal–noise ratio (SNR) as well as large-amplitude multi-components, the energy spectrum cannot yet take effect sufficiently. To optimize the energy spectrum algorithm, the second-order differential of $E_{\mathrm{w}}(u,\xi)$ is obtained by

$$\nabla^2E_{\mathrm{w}}(u,\xi)=\varepsilon\frac{\partial^2E_{\mathrm{w}}(u,\xi)}{\partial u^2}+(1-\varepsilon)\frac{\partial^2E_{\mathrm{w}}(u,\xi)}{\partial\xi^2}. \tag{13}$$

In the equation (13), $\nabla^2E_{\mathrm{w}}(u,\xi)$ represents the second-order differential of $E_{\mathrm{w}}(t,f)$. We define that parameter ε as having two values: 0 and 1, which respectively represent the frequency convexity and time convexity of the targeted signal in the time–frequency domain. In the following research, ε is set to 1 in order to characterize the time-varying feature from the vibration signal.

After the transformation by equation (13), as for the vibration signals, the values will be large at the non-stationary points on the *t–f* plane, and small or close to 0 at the noise points or quasi-steady points. In addition, the values of $\nabla^2E_{\mathrm{w}}(t,f)$ will be positive at the concave points and negative at the convex points. In particular, there are three aspects to be concerned with. First, the second-order differential is often sensitive to noise, which means that many points of zero-crossing are false frequency points and fault frequency spectra [43]. Second, it is hoped that the most noises are suppressed efficiently in order for the targeted IFs to be extracted easily. Third, it is necessary to maintain the useful large-amplitude IFs which mainly represent the useful information of the measured system based on vibration monitoring. Hence it is necessary to reduce such IFs to a certain percentage of the original values as appropriate rather than to be filtered to 0. Because of the above requisition, a novel function by combining the hyperbolic tangent function with the chi-square distribution function in the time–frequency domain is structured as follows:

$$\begin{aligned}Hc_x(u,\xi)=&\alpha\tanh\left(\left|\frac{\nabla^2E_{\mathrm{w}}(u,\xi)}{\nabla^2E_{\mathrm{wfd}}(u,\xi)}\right|\right)\times\left|\nabla^2E_{\mathrm{w}}(u,\xi)\right|\\&+c\chi^2\left(\beta\left|\frac{\nabla^2E_{\mathrm{w}}(u,\xi)}{\nabla^2E_{\mathrm{wfd}}(u,\xi)}\right|;n\right)\times\left|\nabla^2E_{\mathrm{w}}(u,\xi)\right|\end{aligned} \tag{14}$$

where $\tanh(\left|\frac{\nabla^2E_{\mathrm{w}}}{\nabla^2E_{\mathrm{wfd}}}\right|)$ represents the hyperbolic tangent function, and $\chi^2\left(\beta\left|\frac{\nabla^2E_{\mathrm{w}}}{\nabla^2E_{\mathrm{wfd}}}\right|;n\right)$is the chi-square distribution function (χ^2 function) with n degrees of freedom. α,β and c are positive constants. The abovementioned two functions are expressed as follows:

$$\tanh\left(\left|\frac{\nabla^2E_{\mathrm{w}}}{\nabla^2E_{\mathrm{wfd}}}\right|\right)=\frac{2}{1+e^{-2\left|\frac{\nabla^2E_{\mathrm{w}}}{\nabla^2E_{\mathrm{wfd}}}\right|}}-1 \tag{15}$$

$$\chi^2\left(\beta\left|\frac{\nabla^2E_{\mathrm{w}}}{\nabla^2E_{\mathrm{wfd}}}\right|;n\right)=\frac{1}{2^{n/2}\Gamma(n/2)}\left(\beta\left|\frac{\nabla^2E_{\mathrm{w}}}{\nabla^2E_{\mathrm{wfd}}}\right|\right)^{\frac{n}{2}-1}\times\mathrm{e}^{\frac{-\beta\left|\frac{\nabla^2E_{\mathrm{w}}}{\nabla^2E_{\mathrm{wfd}}}\right|}{2}}. \tag{16}$$

Define:

$$p(k)=\alpha\tanh(|k|)+c\frac{1}{2^{n/2}\Gamma(n/2)}(\beta|k|)^{\frac{n}{2}-1}\mathrm{e}^{\frac{-\beta|k|}{2}} \tag{17}$$

$$k=\frac{\nabla^2E_{\mathrm{w}}}{\nabla^2E_{\mathrm{wfd}}} \tag{18}$$

where $p(k)$ is defined as the factor of ET-FSST2. ∇^2E_{wfd} denotes the convexity function of target IF (marked as f_{d}) to be analyzed in the time–frequency domain. The parameter k stands for a specific amplitude value between ∇^2E_{w} and ∇^2E_{wfd}. The absolute value $|k|$ is employed to transfer the negative value to positive. $\Gamma(n/2)$ denotes the Γ function with the n degrees of freedom. In summary, there are four parameters to be calculated: α,β,c,n. The following discussion is focused on how to determine the above four parameters.

3.2. Parameter optimization of the proposed method

Here we present the method of determining the above four parameters which should satisfy three conditions as follows. First, the function $p(k)$ must make $\nabla^2 E_w$ reach its maximum at the f_d and to keep its value unchanged in the transform by equation (14). Second, when $|\nabla^2 E_w| < |\nabla^2 E_{wfd}|$, equation (14) can reduce the values of $|\nabla^2 E_w|$ in order to diminish their interference in the feature of f_d, so $p(k) < 1$ when $0 \leq |k| < 1$. Third, when $|\nabla^2 E_w| > |\nabla^2 E_{wfd}|$, $p(k)$ can reduce the large-value IFs to the certain values for the following two purposes: one is to keep some useful IFs to maintain their features for system state monitoring, and the other is that further untargeted IFs will not submerge the feature of f_d. According to the above analysis, the following conditions need to be satisfied:

$$\begin{cases} \dfrac{\partial p(k_i)}{\partial k_i} = 0 \\ p(k_i) = 1 \\ k_i = 1 \\ \dfrac{\partial p(k)}{\partial k} > 0, k \in (0,1) \\ \dfrac{\partial p(k)}{\partial k} < 0, k \in (1, +\infty). \end{cases} \tag{19}$$

By solving equation (19), the parameters n and c can be expressed as follows:

$$n = 2 + \beta - \frac{8\alpha}{(1+\alpha)(e + e^{-1})^2 - 2\alpha(1 + e^2)} \tag{20}$$

$$c = \frac{2^{\frac{n}{2}} \times \left[(1+\alpha)\left(1 + e^{-2}\right) - 2\alpha\right] \Gamma(n/2)}{\beta^{\frac{n}{2}-1} e^{-\frac{\beta}{2}} (1 + e^{-2})}. \tag{21}$$

In addition, when $k \geq k_0 \geq 1$ (a given constant), $p(k)$ tends to be constant α, which represents the percentage of frequency amplitude after transforming by equation (14). Due to the abovementioned requirement, α should be an adjustive value to determine the percentage (0 –100%) of the large-value IFs to be maintained. Furthermore, the relative error εbetween $p(k)$ and $p(k_0)$ should be small enough. Thus equations (22)~(23) should be satisfied:

$$\lim_{k \to +\infty} p(k) = \alpha \tag{22}$$

$$\lim_{k \to +\infty} \left(\frac{p(k)}{p(k_0)} \right) = 1 - \varepsilon. \tag{23}$$

In our study, it is assumed $\varepsilon = 0.0001$ and $k_0 = 5$ as an example. There are 12 sets of calculated values for contrasting the influence of the values of α and β as examples listed in table 1. Figure 1 shows the different curves when α and β are given to different values as examples. Figure 1(a) shows the different curves of $p(k)$ when $\alpha = 0.2$, and β is given a series of values in the interval of [0,25]. Figure 1(b) illustrates the different curves of $p(k)$ when $\beta = 20$ and α is given to different values in interval of [0,1]. It indicates the main conclusions as follows:

Table 1. Values of the parameters used in ET-FSST2.

Array	α	β	n	c	Array	α	β	n	c
Array 1	0.2	1	2.80	3.27	Array 7	0	20	22.00	15.99
Array 2	0.2	5	6.80	6.83	Array 8	0.2	20	21.80	13.49
Array 3	0.2	10	11.80	9.58	Array 9	0.4	20	21.52	11.01
Array 4	0.2	15	16.80	11.70	Array 10	0.6	20	21.07	8.57
Array 5	0.2	20	21.80	13.49	Array 11	0.8	20	20.28	6.21
Array 6	0.2	25	26.80	15.07	Array 12	1.0	20	18.48	4.09

(1) Although α and β are given series of different values, all of the curves of $p(k)$ reach their maximum when $k = 1$, as we expected. It indicates that concerned IFs maintain their real values exactly in the transform by equations (14)–(18).
(2) The values of the series $p(k)$ descend to 0 when k approaches 0 from either -1 or 1, and this represents that all of the IFs with values satisfying $|\nabla^2 E_w| < |\nabla^2 E_{wfd}|$ (denoted by $|k| \leq 1$) are diminished effectively. By contrast, $p(k)$ descends to a specific constant α and remains steady when $|\nabla^2 E_w| > |\nabla^2 E_{wfd}|$ (denoted by $|k| \geq 1$) as well as satisfying $k \geq k_0 \geq 1$; this means most fast-varying IFs are reduced to a certain percentage (denoted by α) of their original values. Hence, the transform can enhance the feature of weak targeted IFs without adversely affecting the other useful IFs.
(3) The values of α signify the proportion of $\nabla^2 E_w$ that is maintained by the proposed method when $k > k0$. For example, when α=1, $p(k)$ means all of the IFs satisfying $|\nabla^2 E_w| > |\nabla^2 E_{wfd}|$ retain their real values. By contrast,
(4) when α=0, all of the IFs satisfying $|\nabla^2 E_w| > |\nabla^2 E_{wfd}|$ are filtered to 0 and the relatively suitable values of α depend on the actual requisition in application.
(5) The curves of $p(k)$ vary more quickly in the interval [-k0, k0] when β becomes larger. As such, β represents the changing speed of the function $p(k)$.
(6) Because the sharpness and readability of the fast-varying IFs are different because of their varying amplitudes compared to the large IFs of the vibration signal on the t–f plane, k should be adjustive values in the ET-FSST2 to satisfy the feature extracting of different weak components. Here we give a kind of algorithm to roughly evaluate the values of $\nabla^2 E_{wfd}$:

$$k_{0t} = \left\{ \log_2 \left[\max \left(\left| \nabla^2 E_w(u, \xi) \right| \right) \right] \right\} + 1 \tag{24}$$

$$k_t = [1,\ k_{0t}],\ m_t \in Z \tag{25}$$

$$\nabla^2 E_{wfd} = \frac{\nabla^2 E_w}{2^{k_t}} \tag{26}$$

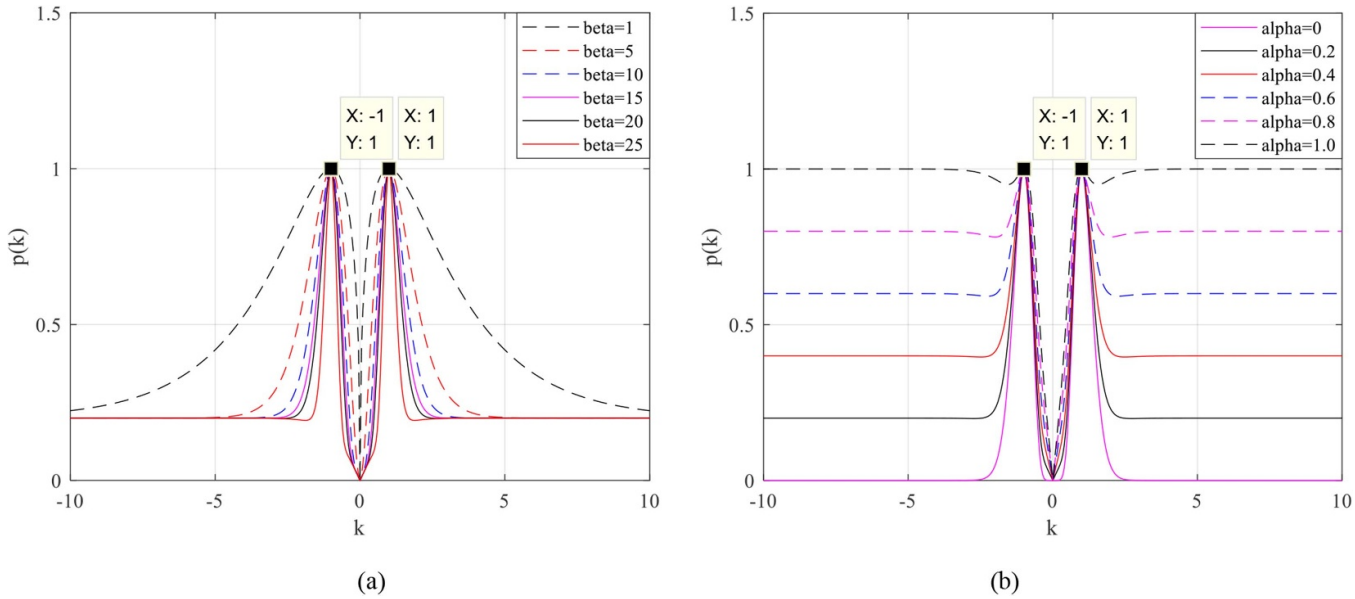

Figure 1. Two examples of $p(k)$: (a) Different values of β when $\alpha = 0.2$, (b) Different values of α when $\beta = 20$.

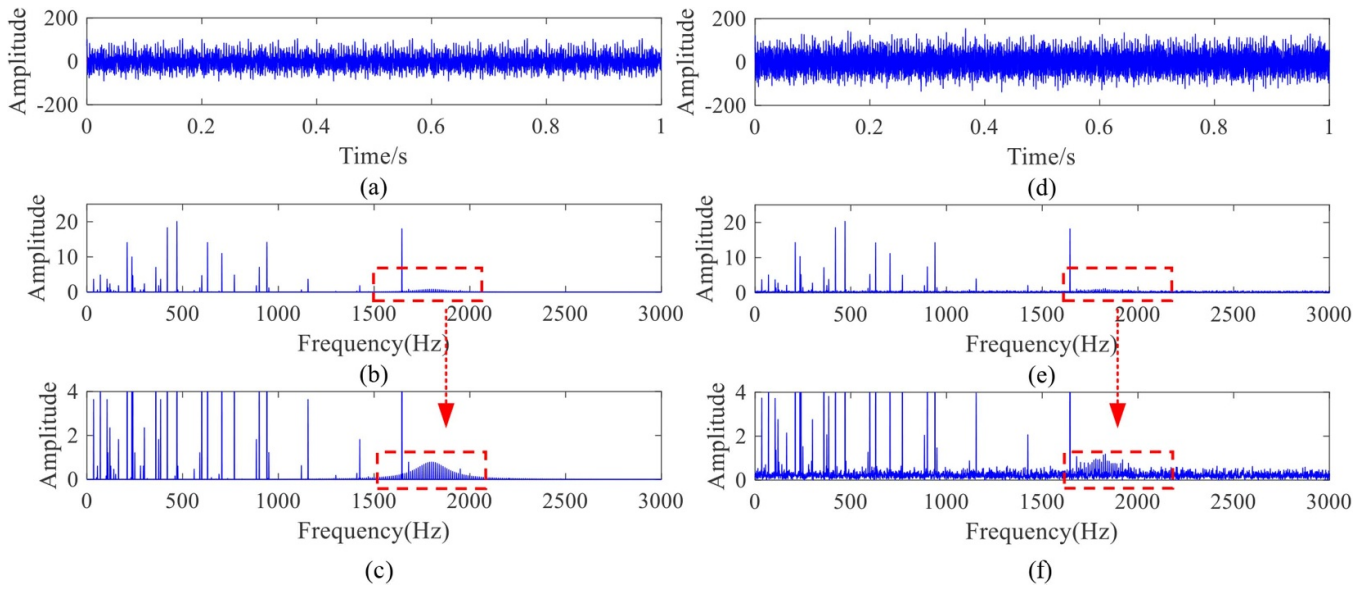

Figure 2. The original signal $s(t)$: (a) in the time domain when $\sigma = 0$, (b) in the frequency domain when $\sigma = 0$, (c) zoomed-in view when $\sigma = 0$, (d) in the time domain when $\sigma = 20$, (e) in the frequency domain when $\sigma = 20$, (c) zoomed-in view when $\sigma = 20$.

where $k_{0\,t}$ represents the orders of $\nabla^2 E_{\mathrm{w}}$ by binary algorithm. $k_{t,}$ which stands for an integer calculated by equation (25), is determined by the actual signal.

3.3. Time–frequency concentration and robustness

In order to measure the time-frequency concentration and readability of the TFRs obtained by the proposed TFA method, the Renyi entropy, which is a tool for testing the information complexity [44], is employed. The probability density function of continuous bivariate $P(x,y)$ with a-order is defined as

$$R_{a,p} = \frac{1}{1-a}\log_2 \iint \left(\frac{P^a(x,y)}{\iint P(x,y)\,dxdy} \right) dxdy. \tag{27}$$

For a TFR $p(t,\ f)$, the Renyi entropy is defined as a pre-normalized function equivalent to normalizing the signal energy to probability density function, and then the Renyi entropy with a-order is defined as

$$R_{a,p} = \frac{1}{1-a}\log_2 \iint \left(\frac{p^a(u,\xi)}{\iint p(u,\xi)\,dud\xi} \right)^a dud\xi. \tag{28}$$

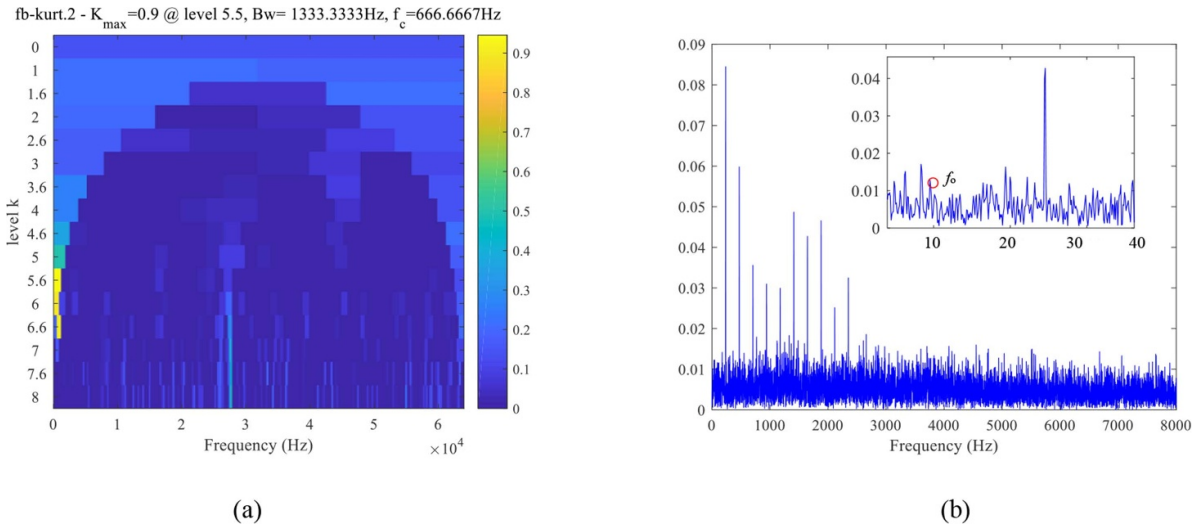

Figure 3. Results of kurtogram for the simulated vibration signal: (a) kurtogram, (b) squared envelope spectrum.

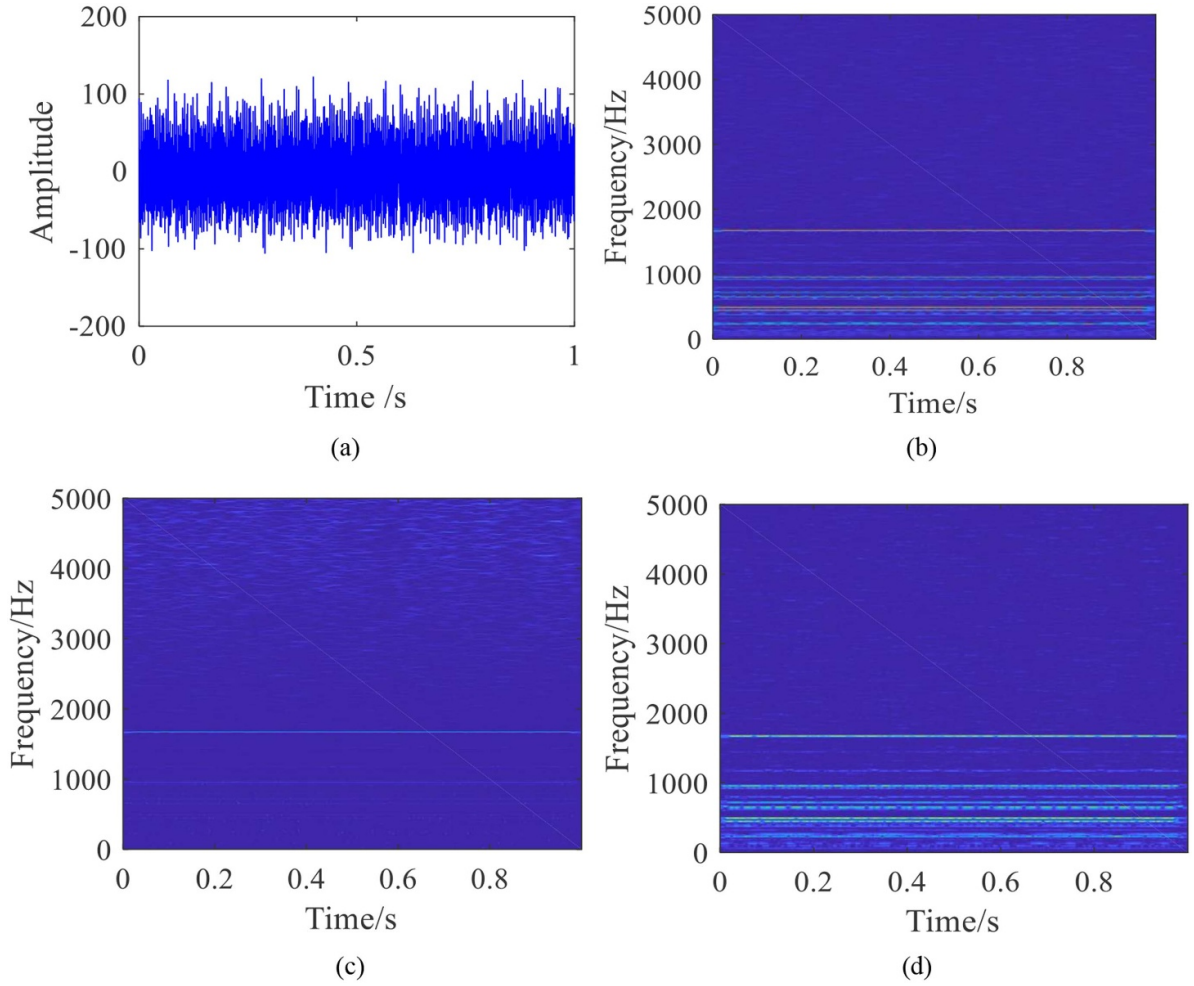

Figure 4. $A_1(t)$ (resonant frequency is 500 Hz as an example): (a) time waveform, (b) FSST2, (c) convexity function in the time direction after FSST2, (d) convexity function in the frequency direction after FSST2.

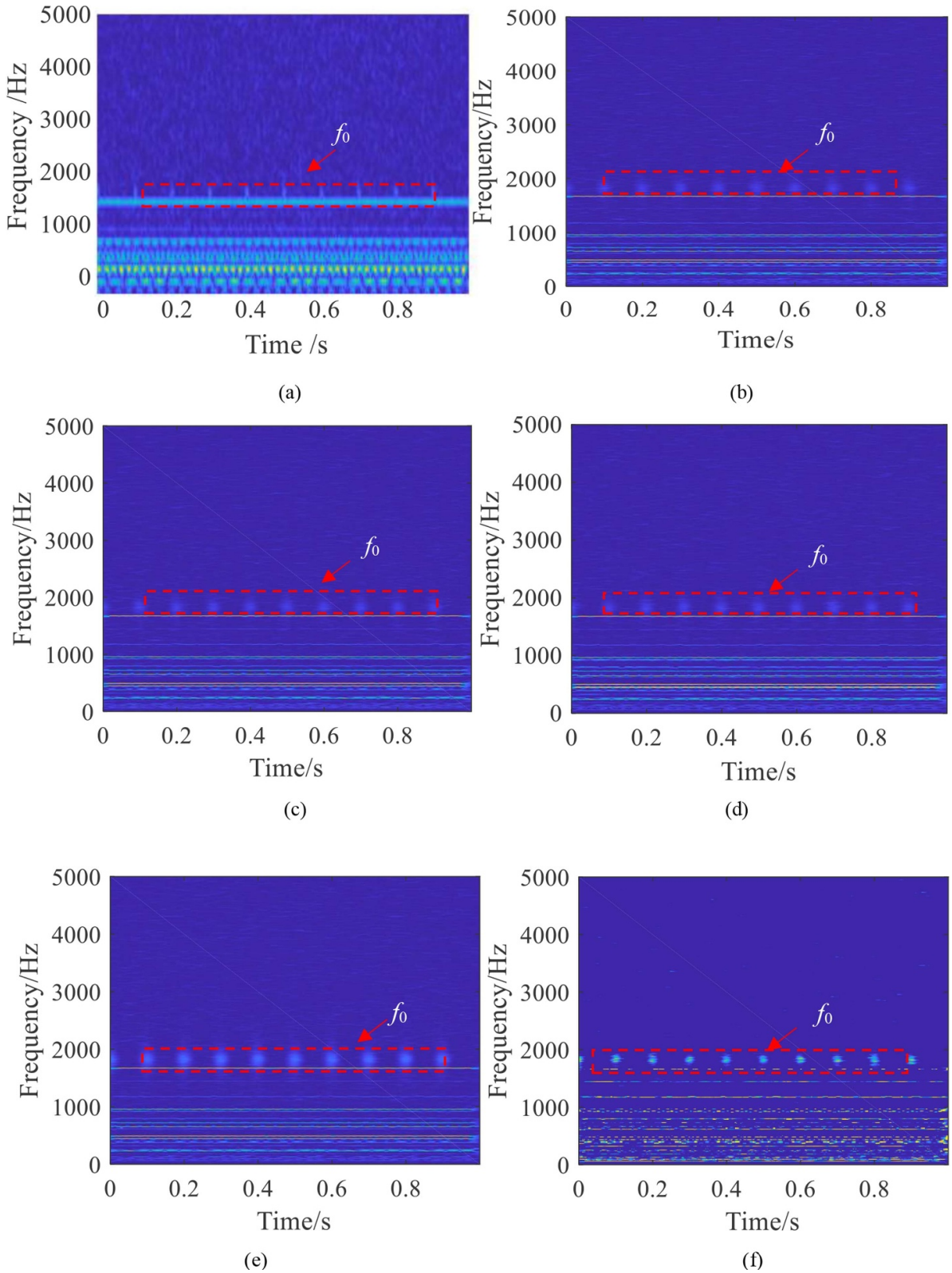

Figure 5. $A_2(t) + a_3(t) + e(t)$: (a) time waveform, (b) FSST2, (c) convexity function in the time direction of FSST2, (d) convexity function in the frequency direction of FSST2.

For testing the robustness of the proposed method, we employ SNR (measured in dB) defined (as usual) by

$$\mathrm{SNR}\,[\mathrm{dB}] = 10\log_{10}\left\{\frac{\mathrm{Var}\,[Hc_0\,(u,\xi)]}{\sigma^2}\right\} \tag{29}$$

where $Hc_0\,(u,\xi)$ is the noiseless signal of $Hc\,(u,\xi)$, and σ is the variance of the background noise.

The above analysis expatiates the proposed method named ET-FSST2. By applying the ET-FSST2 algorithm, the

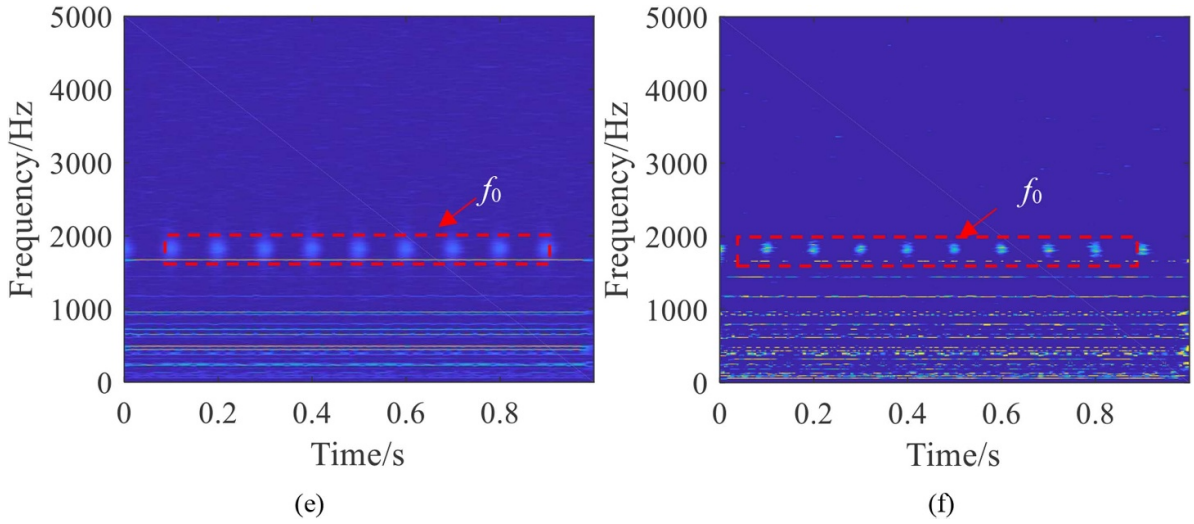

Figure 6. Different TFR for $s_1(t)$ with SNR = 20: (a) STFT, (b) FSST, (c) FSST2, (d) MSST, (e) MDT, (f) ET-FSST2.

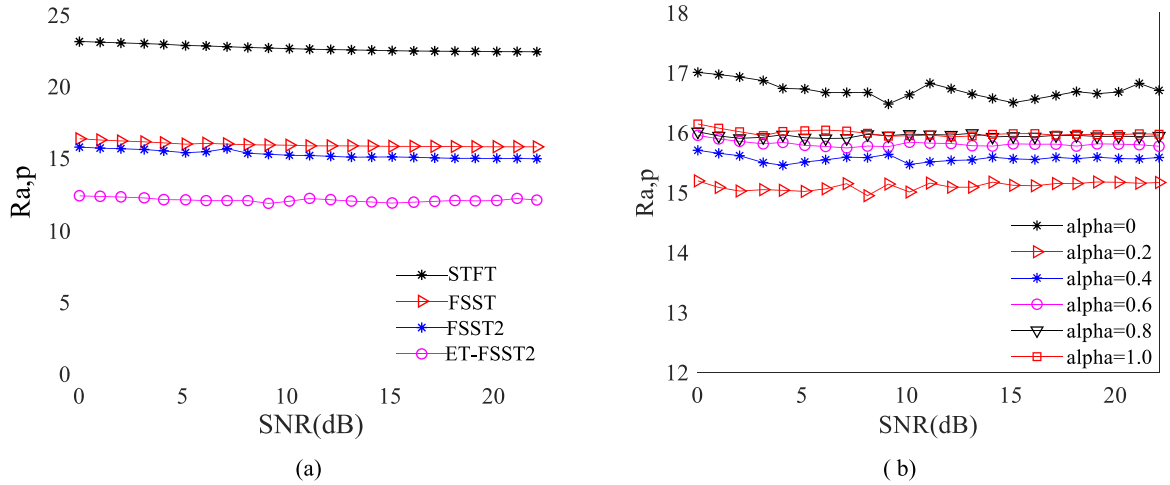

Figure 7. Renyi entropies with different SNR: (a) $\alpha = 0$, $\beta = 20$ for different methods, (b) ET-FSST2 for different values of α when $\beta = 20$.

Table 2. Renyi entropies without the noise.

Algorithm	STFT	FSST	FSST2	MDT	MSST	ET-FSST2
Renyi entropies	22.0332	16.405	15.577	15.601	15.324	13.826

vibration signal will be transformed into the time–frequency domain and be applied for weak fault diagnosis of rolling bearings serviced in aerospace engines, as discussed in section 4. In consideration of the general applicability of the proposed method and diversity of vibration signals, the parameters α, β, k_t should have the ability to satisfy the universalistic application. Hence, we only propose the principle for the parameter selection, and illustrate some values for them in the following study which is employed to show the effectiveness in our study and further preparation for the future research.

4. Numerical experiments for the proposed method

4.1. Simulation study for ET-FSST2

In order to validate the proposed method for extracting the fast-varying IFs with small amplitudes such as impulse-like components from the signal, a simulation signal consisting of four parts is structured as follows:

$$s(t) = a_1(t) + a_2(t) + a_3(t) + e(t) \tag{30}$$

where $a_1(t)$ simulates the periodic impulse-like component of a bearing defect with characteristic frequency being 10 Hz (symbolized as f_0). $a_2(t)$ is the characteristic frequency of a rotor with rotating frequency of 235 Hz (symbolized as f_r), and it also contains multiple components ($2f_r$, $3f_r$, $4f_r$, $4f_r$ and $7f_r$). $a_3(t)$ is the amplitude-modulated and frequency-modulated signal with 3-order, which can increase the complexity for fault feature extraction. Multiples of 90 Hz are the amplitude modulation, and multiples of 175 Hz are the frequency modulation (FM) as well as the carried wave being multiples of 90 Hz. $e(t)$ is the additive zero-mean white noise with standard deviation of variance σ, and σ is given the different values to test the robustness of the compared methods. The sampling frequency is 25.6 KHz. The above four components

of the signals are presented as

$$a_1(t) = \sum_{k1} 1500 \times \sin(2\pi \times 1000)\, e^{-2\pi \times 100t} \sin\left(2\pi \times 1800t - \frac{k_1}{10}\right) \tag{31}$$

$$a_2(t) = 10\sin(2\pi \times 235t + 0.01) + 20\sin(4\pi \times 235t + 0.03) + 11\sin(6\pi \times 235t + 0.02) + 14\sin(8\pi \times 235t + 0.03) + 18\sin(14\pi \times 235t + 0.04) \tag{32}$$

$$\begin{aligned} a_3(t) = {} & 10(1.5 + 0.5\cos(2\pi \times 90t) \\ & \times \cos(2\pi \times 210t + 0.5\cos(2\pi \times 175t)) \\ & + \ +20(1 + 0.5 \times \cos(2\pi \times 180t)) \\ & \times \cos(2\pi \times 420t + 0.5 \times \cos(2\pi \times 350t)) \\ & + 30(2 + 0.5 \times \cos(2\pi \times 270t)) \\ & \times \cos(2\pi \times 630t + 0.5 \times \cos(2\pi \times 525t)) \end{aligned} \tag{33}$$

$$e(t) = \sigma \times \mathrm{random}(m). \tag{34}$$

The simulated signal in the time domain and frequency domain is illustrated in figure 2. In order to test the performance of the ET-FSST2 algorithm in intensive background noise, σ is given two values: 0 and 20. It indicates that the noise almost submerges the impulse-like component when σ= 20, and other IFs such as the rotating frequency and harmonic components are larger than the impulse-like component. Hence, the fault frequency component cannot be identified easily by FFT.

A fast kurtogram (FK), a common tool for mechanical signal processing, is employed to test the effectiveness of the weak fault feature extraction from the simulated signal. Figure 3 presents the fast kurtogram (FK) and the squared envelope spectrum of the simulated signal when $\sigma = 20$. It indicates that the optimal filtering center spectrum and optimum bandwidth are 1333.33 Hz and 666.67 Hz respectively, and the feature of f_0 is not very clear. Hence the characteristic of f_0 cannot be shown obviously by the FK algorithm.

4.2. Time–frequency characteristic by the ET-FSST2

In the investigation of simulation for the proposed algorithm in this section and its application in section 5, the Kaiser window is selected as the window function. As far as studies have reported, the Kaiser window is a kind of optimal window the main lobe of which concentrates most of the internal energy of the frequency band, and it can exert the greatest inhibition on the side lobe [45, 46]. Meanwhile, the coefficients of the Kaiser window and the length of the window function are selected as the same values respectively in the comparison of the algorithm simulation, as well as the three application cases, so it can further ensure that the employed TFA methods are compared under the same conditions.

In order to test the effectiveness of the convexity function for the impulse IF and quasi-steady state IF from the signal, the second-order derivatives in the time and frequency directions of $a_1(t)$ and the signal $a_2(t) + a_3(t) + e(t)$ are calculated respectively. Both $a_1(t)$ and $a_2(t) + a_3(t) + e(t)$ are transformed into the time–frequency domain by FSST1, FSST2 and second-order derivatives. Figures 4(c)–(d) show the convexity function of $a_1(t)$ when the resonant frequency is set to 500 Hz as an example in the time and frequency directions, and the time-varying characteristics in these directions are still clear after the two-order derivatives transform on the *t–f* plane. By contrast, figures 5(c)–(d) illustrate the IF representation of $a_2(t) + a_3(t) + e(t)$ which represents an example of the quasi-steady state components almost being filtered by calculating the second-order derivatives in the time direction, and the FM components are blurred by some mutational points. By contrast, the large-amplitude IFs of $a_2(t) + a_3(t) + e(t)$ still remain in the frequency direction. Hence, it is validated that the algorithm can be employed to extract time-varying components such as impulse-like IF from the signal. As such, it also clarifies the essence that we adopt a convex function in the time direction rather than in the frequency direction.

For the purpose of further exploring the effectiveness of different TFR methods for weak fast-varying IF extraction, the simulation signal is analyzed by some TFR methods such as STFT, FSST, FSST2, MDT, MSST and the proposed method, as shown in figure 6. All of the above methods employ the same window function, and the parameters are given as α = 0, $\beta = 20$, $k_t = 3$ as an example. It can be seen that the TFR obtained by STFT is blurred, and the impulse-like IF cannot be clear. While the IFs are sharpened by FSST, FSST2 MDT and MSST, the weak impulse component is submerged to some extent by large-value IFs. After applying the ET-FSST2, the weak impulse is concentrated, and its wide-band frequency and time-decay characteristics are both displayed obviously.

4.3. Energy concentration and robustness

The robustness is a critical index for TFR methods. In order to study the influence of the background noise on ET-FSST2, σ is given as large as 20. Figure 7 gives the signal in the time–frequency domain of ET-FSST2; the IF of an impulse-like component on the *t–f* plane is blurred by employing STFT but still obvious by ET-FSST2, as shown in figures 6(a) and (c).

Energy concentration is significant to evaluate the performance of the method which is often measured by Renyi entropies. Figure 7 illustrates the Renyi entropies under different SNR when α= 0, β = 20 and a = 3 as an example. Table 2 shows the Renyi entropies of noiseless signals. The Renyi entropies of FSST2, MDT and MSST are similar, namely 15–16, not as large as FSST. By contrast, the Renyi entropies of ET-FSST2, which is smaller than other algorithms, represents the lowest information complexity.

In summary, the result of the simulation signal indicates that the ET-FSST2 algorithm outperforms the STFT, FSST

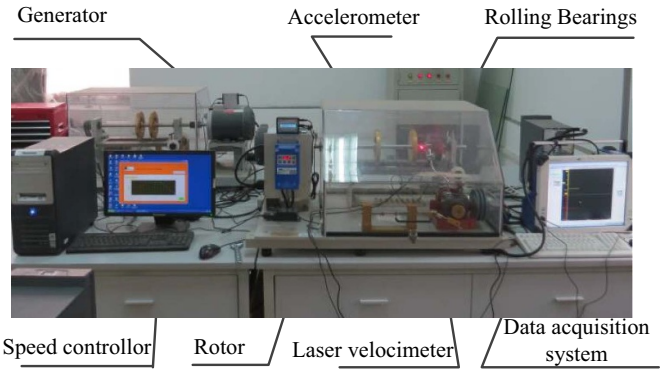

Figure 8. The fault experiment of rolling bearings

Figure 8. Fault experiment of a rolling bearing.

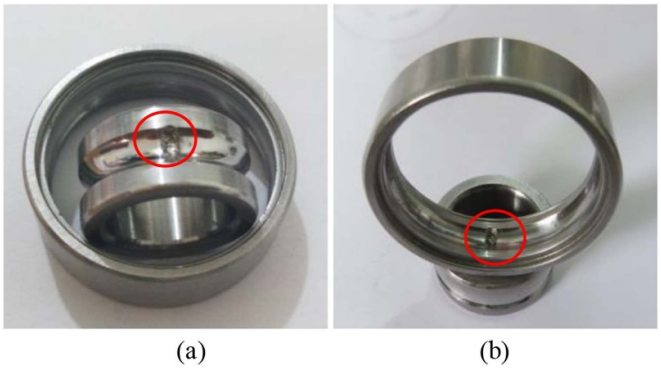

Figure 9. Manufactured defect of bearings: (a) IRF, (b) ORF.

Table 3. Characteristic frequency of the tested bearings.

Frequency	Value/Hz	Frequency	Value/Hz
IRF/f_i	108.64	ORF/f_o	71.44

and FSST2, MDT and MSST in feature extraction of small-amplitude fast-varying IFs such as impulse-like components. Furthermore, the ET-FSST2 algorithm is robust under background noise. Hence, the simulation results provide valuable pre-validations for follow-up research on the diagnosis of rolling bearings serviced in aerospace engines.

5. Application in fault diagnosis of rolling bearings serviced in aerospace engines

5.1. Case 1: application to defect diagnosis on the ring race of rolling bearings

In order to validate the effectiveness of the proposed method for weak IF extraction from the large-amplitude multi-components, an experiment for testing the performance of the fault rolling bearings was held. Vibration signals from a motor bearing test rig were recorded. The test rig contained (see figure 8) a generator, a rotor system, speed controller, laser velocimeter, data acquisition system and rolling bearings. The motor speed could be adjusted by an installed speed controller. The tested bearings are ER16 K type, which were manufactured with single-point defects, such as outer race fault (ORF), inner race fault (IRF), and rolling element fault (REF). An accelerometer was installed vertically on the drive end and signals were recorded by data acquisition. The testbed and the fault bearing are shown in figures 8 and 9 respectively.

Looking at the results of figure 10, it is worth noting that the qualities of TFR are quite different after applying the different methods. The characteristic of the bearing defect on the t–f plane are still blurred by employing STFT, FSST and FSST2. In the ET-FSST2, the parameters $\alpha = 0.2$, $\beta = 20$ and $k_t = 3$ as examples. Although there are plenty of time-varying components enhanced during the transform on the t–f plane, it clearly interprets that ET-FSST2 can enhance the weak fault IF compared to other TFA methods.

In this section, through the conventional verification for the rolling bearing fault diagnosis, it can be concluded that the ET-FSST2 surpasses other TFA algorithms such as STFT, FSST and FSST2 in diagnosing the weak fault of rolling bearings based on vibration signals.

5.2. Case 2: application to Ni–Cu–Ag PVD coating exfoliation diagnosis of rolling bearing in aerospace engines

5.2.1. Introduction of the cryogenic test In accordance with the working condition of a rolling bearings serviced aerospace engine, a cryogenic experiment was carried out to test the performance of the abovementioned bearings. The testbed (see figure 11) consisted of a tested bearing, two service bearings, a driving system, an axial loading equipment, a radical loading equipment, coupling, and an LN_2 supplying system. The axial load was exerted on the shaft which connects with the service bearing on the left of the tested bearings. The driving system was mainly composed of a turbine and appurtenance. The turbine was driven by high-pressure air. The LN_2 supplying system could provide LN_2 at high pressure, mass flow and cryogenic temperature. During the experiment, the temperature of LN_2 in the inner cavity was steadied at 85–90 K initially. Then, the system was driven by the air turbine. Besides, the feature frequencies of the tested bearings are listed in table 3. When the rolling speed reached the designed value, the loads were exerted on the service bearing. In the test, three vibration accelerometers in the orthogonal direction were set on the outer shell surface and a temperature sensor was installed on the outer ring of the tested bearings. The experiment lasted about 120 s for each bearing. The sampling frequency was 25.6 KHz. The data was obtained by special cryogenic temperature vibration sensors. Meanwhile, the signal was sampled by NI-9234 C and GETAC S41O with the Inter Core i7-8550 U. Each bearing sample was tested under the same conditions as illustrated in table 4.

After the experiment, the tested bearings took a different appearance on the surface by using microscopes of 500 times magnification. Some Ni–Cu–Ag PVD coatings on the

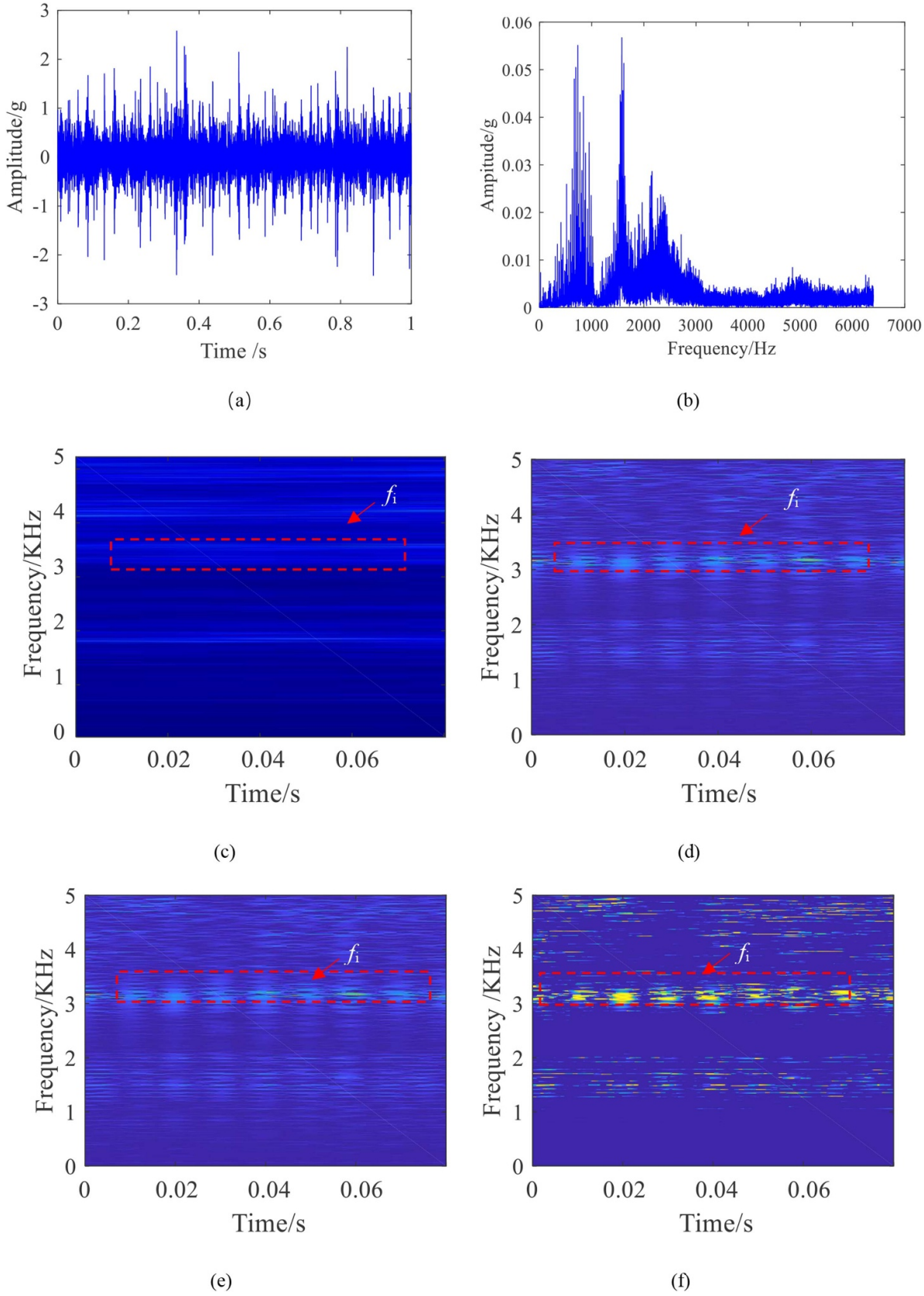

Figure 10. Result of IRF signal for tested bearing: (a) signal in the time domain, (b) signal in the frequency domain, (c) STFT, (d) FSST, (e) FSST2, (f) ET-FSST2.

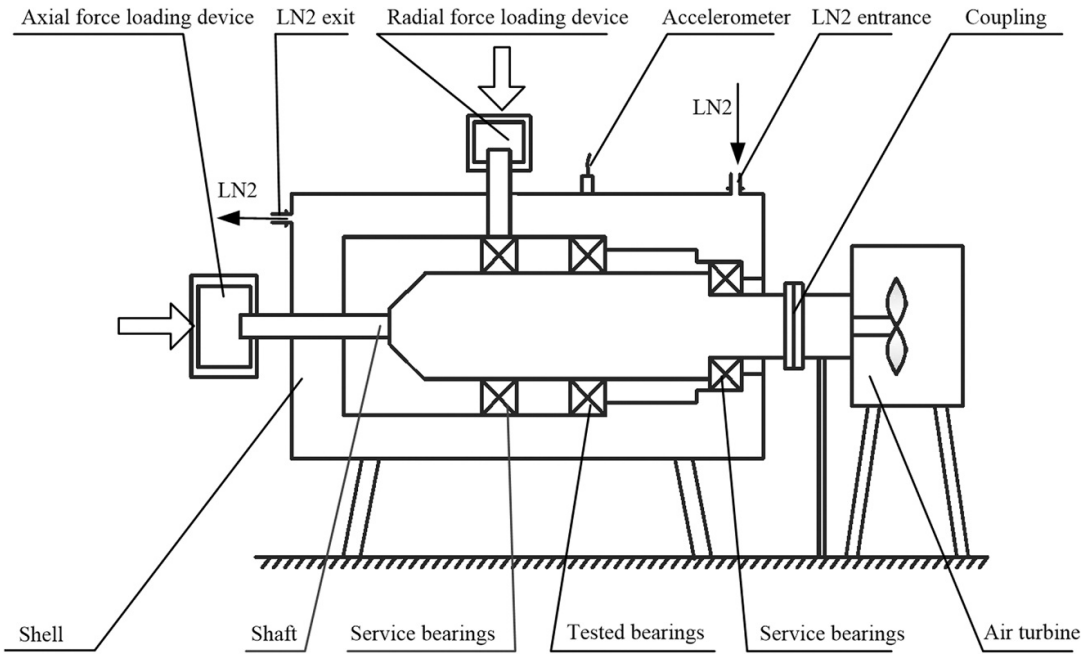

Figure 11. Rolling bearings running experiment in LN2.

Table 4. Conditions of the rolling bearings and experiment.

Items	Value	Items	Value
Style	Angular contact	LN_2 pressure	3.0–5.0 MPa
Material	9Cr18	LN_2 temperature	85–90 K
Coating material	Ni–Cu–Ag	Rolling speed/f_r	14 000 $\pm$ 200 rpm
Coating thickness	10 μm	IRF/f_i	7.03 f_r
ORF/f_i	5.31f_r	REF/f_e	2.70f_r

inner ring of other bearings exfoliated as shown in figure 12. Moreover, there were some surface scratching-like defects on the outer ring of some tested bearings. In order to validate the effectiveness and generality of the proposed method for weak impulse-like signal processing as well as fault diagnosis, the above two kinds of defects were both analyzed by several TFA methods, detailed in section 5.2.2 and section 5.3 respectively.

5.2.2. Time–frequency characteristic by the ET-FSST2 algorithm The vibration signal in the time domain and frequency domain (by FFT) is illustrated in figure 13, on which the health state of the tested bearings cannot be estimated directly. This is because the mass flow of LN_2 and its high flow velocity lead to fierce vibration and plenty of noise. By contrast, the vibration caused by Ni–Cu–Ag PVD coating exfoliation of the tested bearing is relatively weak. The proposed method is compared with FK, STFT, FSST, FSST2, MDT and MSST for feature extraction. To clarify the essence of the above algorithm, the results are discussed as follows.

FK is applied to calculate the kurtosis index, and the impulse components are extracted and highlighted after the raw signal is processed by the band filter of which the center frequency and bandwidth are optimized. Figure 14 presents FK and the squared envelope spectrum of the simulated signal. It indicates the optimal filtering center spectrum is 333.33 Hz, and the optimum bandwidth is 166.67 Hz. As shown in figure 14(b), the feature of f_0 is unclear. Hence, the component of the impulse fault caused by Ni–Cu–Ag PVD coating exfoliation is not effectively extracted by FK.

ET-FSST2 is compared with traiditional TFA algorithms such as STFT, FSST, FSST2, MDT and MSST for extracting weak fault IFs from the complex multi-component vibration signal. Figure 15 shows the diagnosis results of ORF caused by Ni–Cu–Ag PVD coating exfoliation of the tested bearings, and $\alpha = 0.2$, $\beta = 20$ (as an example), $f_0 = 1238$ Hz, and $k_t = 1$. This indicates that the noises are very complicated by STFT, and the feature of f_0 cannot be detected directly (see figure 15(a)). Although the noises are suppressed partially by FSST, there are still plenty of high-amplitude IFs which submerge the feature of f_0. By contrast, in spite of the characteristics of f_0 shown by FSST2, MDT and MSST being clear to some extent on the *t–f* plane as illustrated in figures 15(c)–(e), there is still some noise, and the impulse characteristics are not depicted obviously. After employing the proposed method, the noise is effectively suppressed, and the features of the fault IFs are shown clearly. In order to further explore the difference between the FSST2 and its theoretical basis method, namely FSST, the segment spectrum in the frequency direction is given (see figure 16). It can be regarded as an auxiliary analysis for the TFA methods. Taking the fault point P (0.03625 s, 1238 Hz) for example, the amplitude is only 4.24, which is overflowed under the noise by adopting FSST2. However, the amplitude of f_0 is 86.99 which is still obvious by employing

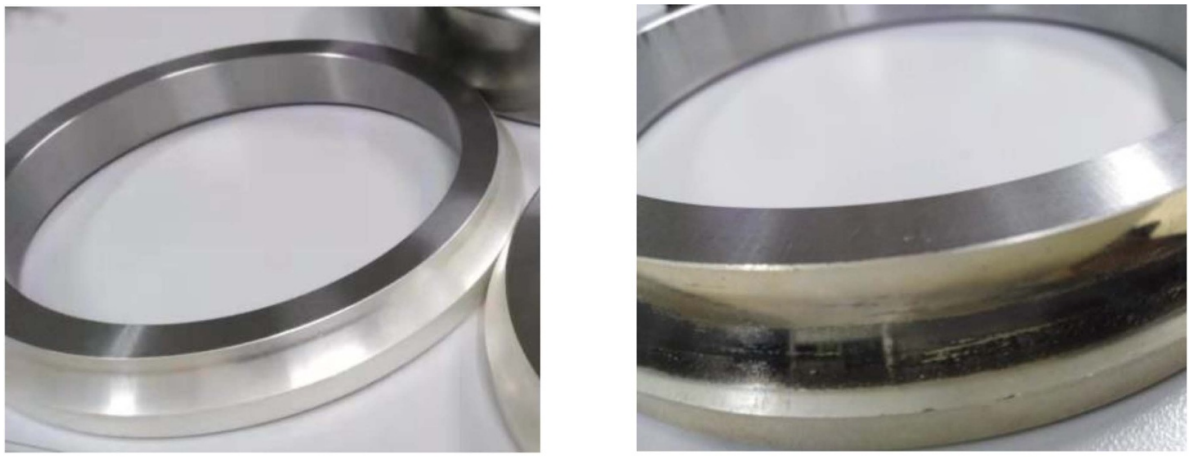

Figure 12. Rolling bearings after experiment: (a) normal inner ring, (b) exfoliation of the Ni–Cu–Ag coating on the inner ring.

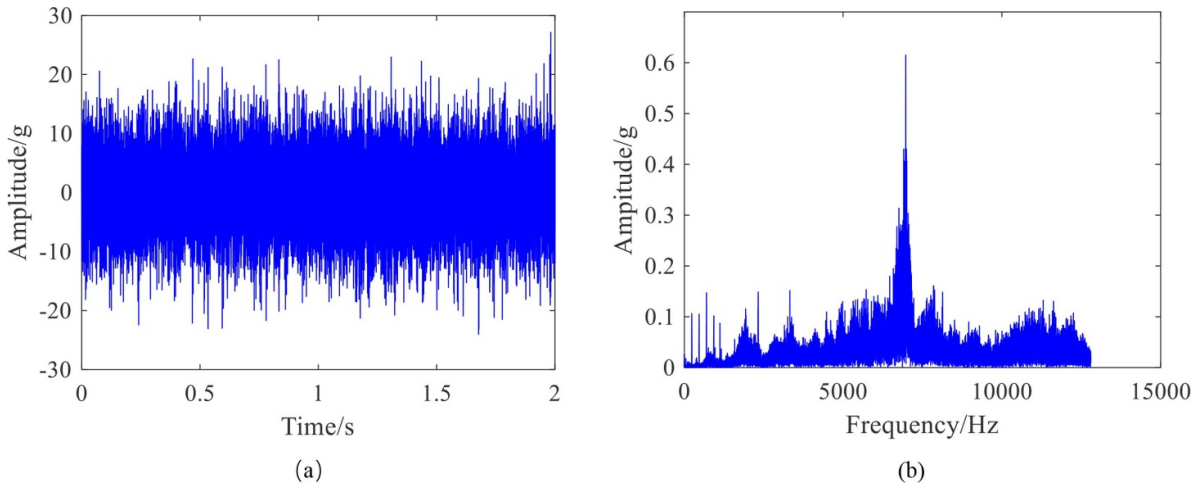

Figure 13. Original vibration signal of the tested rolling bearing: (a) in the time domain, (b) in the frequency domain.

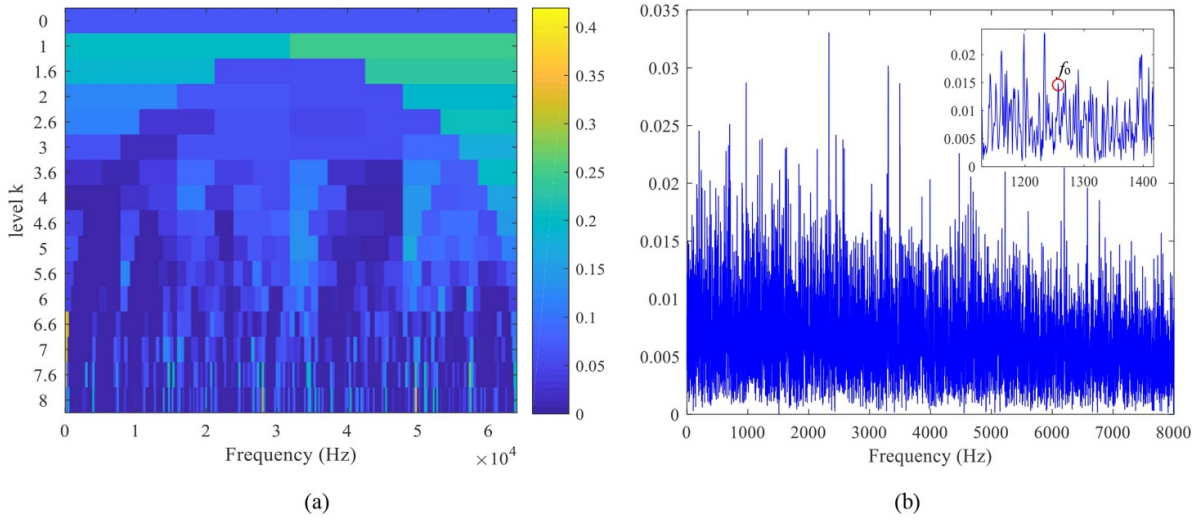

Figure 14. Results of the kurtogram for vibration signal of the tested bearings: (a) kurtogram, (b) squared envelope spectrum.

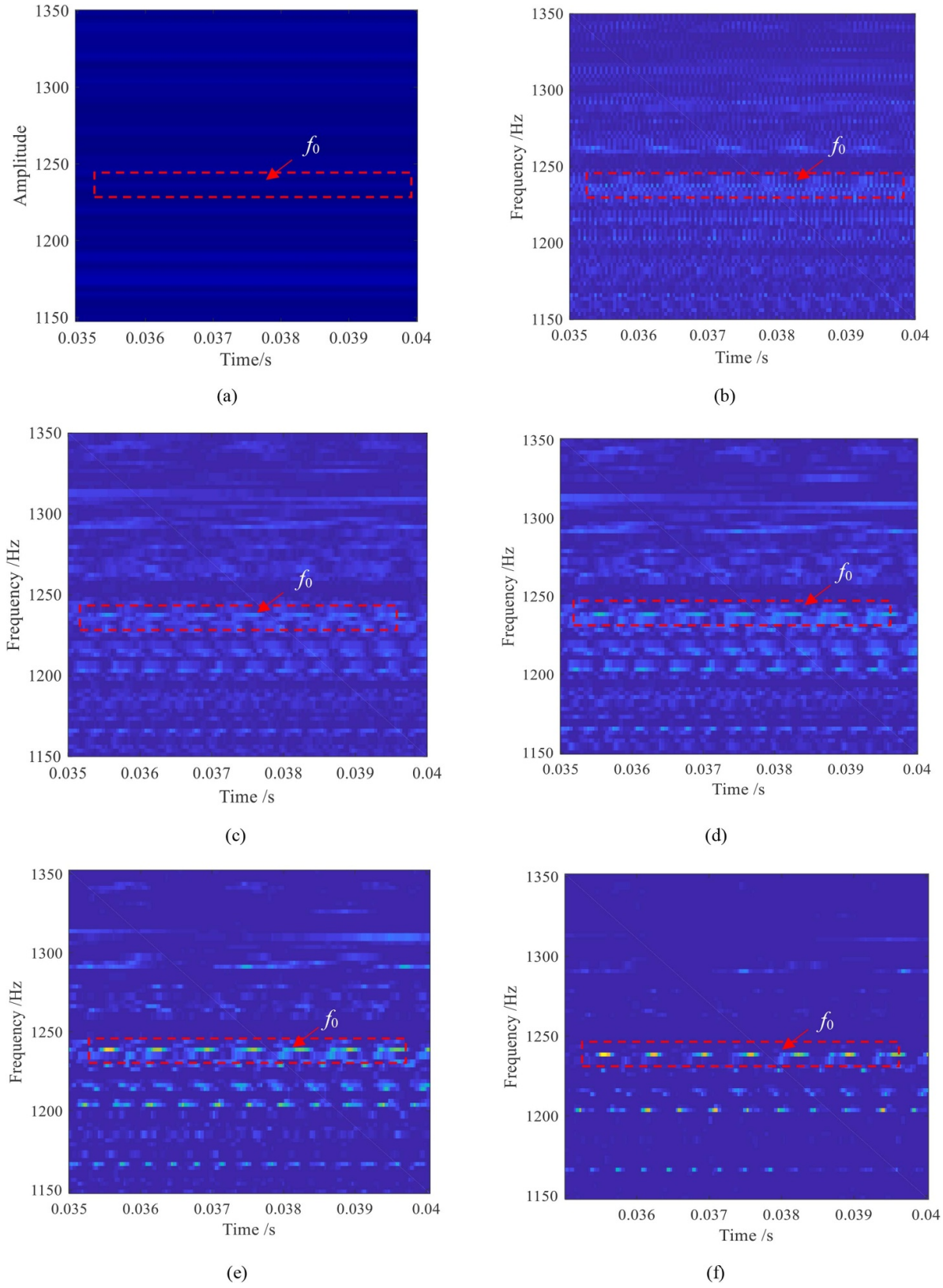

Figure 15. Time–frequency image of Ni–Cu–Ag PVD coating exfoliation on the outer ring: (a) STFT, (b) FSST, (c) FSST2, (d) MDT, (e) MSST, (f) ET-FSST2.

ET-FSST2, and most frequency components which are unrelated to f_0 are reduced effectively, as shown in figure 15(f). Consequently, the feature of f_0 is more obvious than FSST2.

Energy concentration is employed to test the performance of the signal processing result. Figure 17 gives the Renyi entropies of the different methods when the coefficients α and

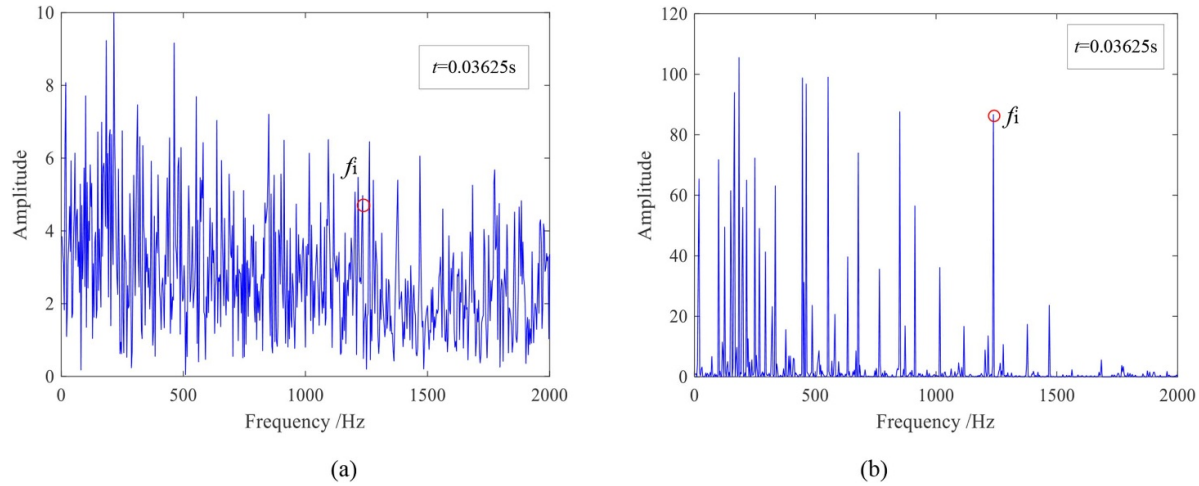

Figure 16. Frequency spectrum of the FSST2 and ET-FSST2 when $t = 0.03625$ s: (a) FSST2, (b) ET-FSST2 ($\alpha = 0.2$, $\beta = 20$).

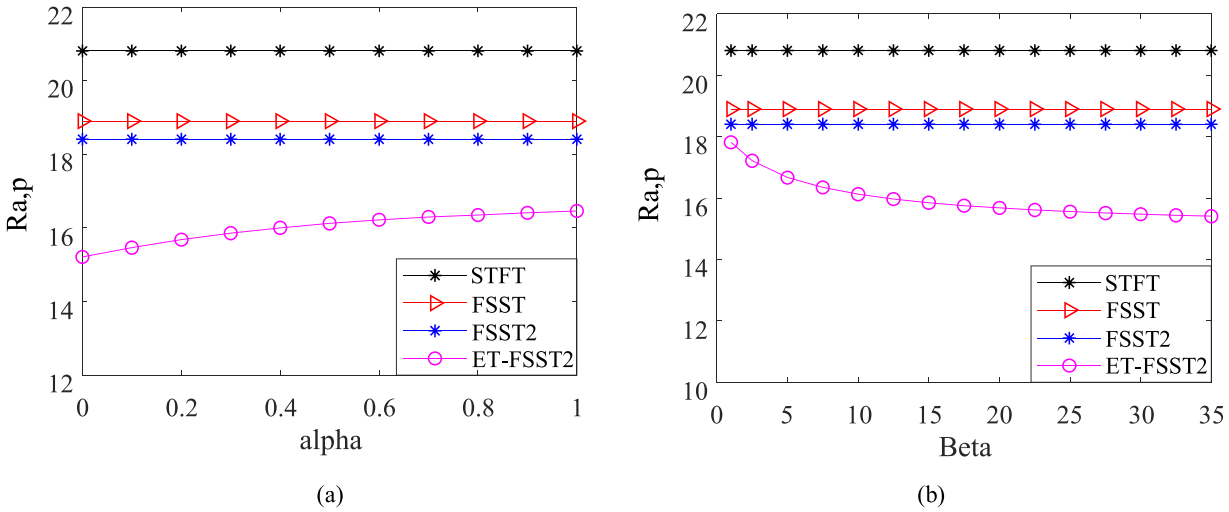

Figure 17. Renyi entropies of different α and β: (a) α, (b) β.

β are given different values and $a = 3$. It indicates that the ET-FSST2 algorithm has the smallest entropies in comparison with the other methods in the time–frequency domain. When $\alpha = 0.2$ and β is given a series values between 1 and 50, the Renyi entropy is steadied in the range of 17.82–15.41. In addition, when $\beta = 20$ and α is given a series of values between 0 and 1, the Renyi entropy is steadied in the range of 15.21–16.46 while the Renyi entropies of the other methods are more than 18.40, especially by STFT. Hence, the energy concentration in the time–frequency domain by ET-FSST2 is improved compared to the other methods.

5.3. Case 3: application to scratching-like defect diagnosis of rolling bearings under cryogenic temperature in aerospace engines

The process and conditions of the scratchings test for the rolling bearings at cryogenic temperature is same as the experiment described in section 5.2.1, and the rotating speed is set to 15 000–15 500 rpm. After the test, there are some surface scratching-like defects in the circumferential direction of the outer ring for some tested bearings. It is clearly visible as shown in figure 18.

To validate the performance of the proposed methods for scratching detection, the vibration signals under crygenic temperature of the rolling bearings are analyzed by FSST2, MDT, MSST and ET-FSST2. The results are shown in figure 19. Because of the fierce vibration, strong noises and mass flow of the LN_2 during the cryogenic experiment, the features of the impulses caused by scratchings are to some extent blurry on the t–f plane in spite of employing FSST2 and MSST (see figure 19). By contrast, the fault characters of f_i are easily found on the t–f plane by adopting ET-FSST2. Moreover, the wide-frequency character and the attenuation feature are also found clearly.

Table 5 lists the Renyi entropies of the different methods when $a = 3$, and the Renyi entropies of the three compared methods are 13–15. As such, the value is smallest

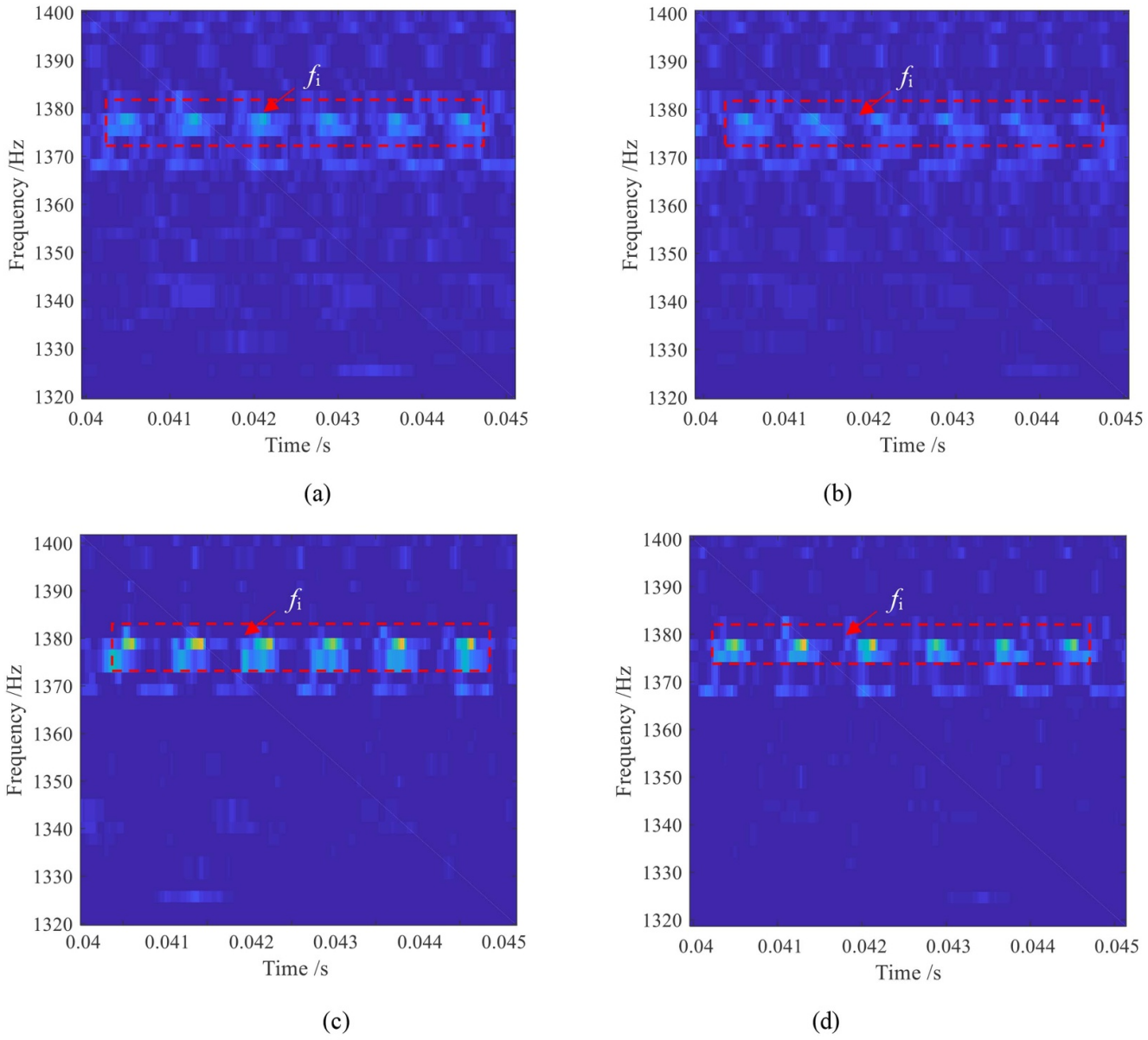

Figure 18. (a) Tested bearing, (b) scratching-like defect on the outer ring.

by employing the ET-FSST2, which represents the the lowest information complexity and the highest energy concentration.

In summary, the ET-FSST2 algorithm has an advantage over the FSST like FSST2, MDT and MSST in improving the energy concentration of time-varing signals. More importantly, it can enhance the weak impulse-like component from the vibration signals. Additionally, in this section, the proposed method is further validated effctively in some kinds of weak fault detection such as exfoliation of Ni–Cu–Ag coatings and the scratching-like defects of the rolling bearings serviced in aerospace engines under fierce vibration.

6. Conclusion

In this study, a TFA method named ET-FSST2 is proposed for extracting the time-varying IFs with small amplitudes from multi-component vibration signals. The ET-FSST2 is presented first, followed by numerical simulation and bearing fault tests to validate its effectiveness, energy concentration and robustness. After this, cryogenic experiments are carried out to test the effectiveness of ET-FSST2 for diagnosing the performance of rolling bearings serviced in aerospace engines. Based on the study, the main conclusions are listed as follows:

(a) In addition to retaining the advantage of FSST2 in energy concentration of TFR, ET-FSST2 can extract the non-stationary IFs by calculating the energy convexity function in the time direction after FSST2. More importantly, it can extract the weak components of the non-stationary IFs by structuring an optimization function consisting of a hyperbolic tangent function and chi-square distribution function.

(a) (b)

Figure 19. TFA result of scratchings of rolling bearings in a cryogenic test: (a) FSST2, (b) MDT, (c) MSST (d) ET-FSST2.

Table 5. Renyi entropies of TFA methods for scratching detection.

Algorithm	FSST2	MDT	MSST	ET-FSST2
Renyi entropies	15.613	15.573	14.324	13.698

(b) The simulation and rolling bearing tests show that the proposed method has good robustness under complex background noise. It has the smallest Renyi entropy in comparison with the traditional TFA algorithms, such as STFT, FSST, FSST2, MDT and MSST, and also reduces the complexity of the vibration signal.

(c) For the application of the ET-FSST2 algorithm, it can diagnose weak faults such as exfoliation of coatings and scratching-like defects of the rolling bearings working in aerospace engines. Furthermore, it has the potential to be generalized in the fields of mechanical signal processing, health monitoring and fault diagnosis.

Acknowledgments

This work is supported by the National Natural Science Foundation of China (Grant Nos. 61633001 and 51775411), The authors would like to thank Mr. Jin, Mr. Niu, Dr. Li and the other experimental assistants in the Xi'an Aerospace Propulsion Institution (China Aerospace Science and Technology Corporation), who have given us great help in the cryogenic experiment process.

ORCID iDs

Yanyang Zi https://orcid.org/0000-0002-3045-6514
Jinglong Chen https://orcid.org/0000-0002-9805-9849

References

[1] Shan Q, Bradford A S and Dewhurst 1998 New field formulas for the Fabry–Perot interferometer and their application to ultrasound detection *Meas. Sci. Technol.* **9** 24–37

[2] Wang Q Y, Zhang Z L, Wang Z Y and Zhou W H 2016 The trajectory prediction of spacecraft by grey method *Meas. Sci. Technol.* **27** 085011

[3] Eiden M and Seiler R 2004 Space mechanisms and tribology challenges of future space missions *Acta Astronaut.* **55** 935–43

[4] Zhang G, Yuan X and Dong G 2010 The tribological behavior of Ni–Cu–Ag-based PVD coating for hybrid bearings under different lubrication conditions *Tribol. Trans.* **43** 197–201

[5] Hall P B, Thom R and Chang L 1997 An experimental/analytical study of high-speed, high-load rolling/sliding contacts with ultra-low viscosity fluids *Tribol. Trans.* **40** 41–8

[6] Chase T J 1993 Wear modes active in angular contact ball bearings operating in liquid environment of the space shuttle turbopumps lubrication engineering *Lubr. Eng.* **49** 313–22

[7] Bouzakis K D, Vidakis N, Lontos A, Mitsi S and David K 2000 Implementation of low temperature-deposited coating fatigue parameters in commercial roller bearings catalogues *Surf. Coat. Technol.* **133–4** 489–96

[8] Lei S 1996 Investigation and corrective actions of foreign space launch vehicle catastrophic failures *Spacecr. Recovery Remote Sens.* **17** 59–66

[9] Miao X S, Hu M, Li A M, Wang D S, Weng L J, Li X Y and Zhang G 2018 Investigation on the lubricity of self-lubricating ball bearings for cryogenic turbine pump *Tribol. Int.* **121** 45–53

[10] Choe B, Lee J, Jeon D and Lee Y 2019 Experimental study on dynamic behavior of ball bearing cage in cryogenic environments, Part I: effects of cage guidance and pocket clearances *Mech. Syst. Signal Process.* **115** 545–69

[11] Qin Y, Xing J F and Mao Y F 2016 Weak transient fault feature extraction based on an optimized morlet wavelet and kurtosis *Meas. Sci. Technol.* **27** 085003

[12] Ming Y, Chen J and Dong G M 2011 Weak fault feature extraction of rolling bearing based on cyclic Wiener filter and envelope spectrum *Mech. Syst. Signal Process.* **25** 1773–85

[13] Nosaka M, Takada S, Kikuchi M, Sudo T and Yoshida M 2004 Ultra-high-speed performance of ball bearings and annular

seals in liquid hydrogen at up to 3 million DN (120,000 rpm) *Tribol. Trans.* **47** 43–53
[14] Monicault J-M D, Garceau P, Vagnard G 1991 Oxygen compatibility of materials and equipment for the Vulcain European rocket engine *J.ASTM Int.* **49** 475–88
[15] Wu W J and Huang D G 2011 Research on fault diagnosis for rotating machinery vibration of aero-engine based on wavelet transformation and probabilistic neural network *CIRP J. Manuf. Sci. Technol.* **295–7** 2272–8
[16] Rinaldi G, Stiharu I, Packirisamy M, Nerguizian V, Landry R Jr and Raskin J-P 2010 Dynamic pressure as a measure of gas turbine engine (GTE) performance *Meas. Sci. Technol.* **21** 045201
[17] Brandt A 2019 A signal processing framework for operational modal analysis in time and frequency domain *Mech. Syst. Signal Process.* **115** 380–93
[18] Chang J, Kim M and Min K 2002 Detection of misfire and knock in spark ignition engines by wavelet transform of engine block vibration signals *Meas. Sci. Technol.* **13** 1108
[19] Pachori R B and Nishad A 2016 Cross-terms reduction in the Wigner–Ville distribution using tunable-Q wavelet transform *Signal Process.* **120** 288–304
[20] Jiang H, Xia Y and Wang X 2013 Rolling bearing fault detection using an adaptive lifting multiwavelet packet with a 11 2 dimension spectrum *Meas. Sci. Technol.* **24** 125002
[21] Zhao M H, Tang B P and Tan Q 2015 Fault diagnosis of rolling element bearing based on S transform and gray level co-occurrence matrix *Meas. Sci. Technol.* **26** 085008
[22] Dragomiretskiy K and Zosso D 2014 Variational mode decomposition *IEEE Trans. Signal Process.* **62** 531–44
[23] Meignen S, Pham D H and McLaughlin S 2017 On demodulation, ridge detection, and synchrosqueezing for multicomponent signals *IEEE Trans. Signal Process.* **65** 2093–103
[24] Yu G 2020 A concentrated time–frequency analysis tool for bearing fault diagnosis *IEEE Trans. Instrum. Meas.* **69** 371–81
[25] Yu K, Lin T R, Ma H, Li H F and Zeng J 2020 A combined polynomial chirplet transform and synchroextracting technique for analyzing nonstationary signals of rotating machiner *IEEE Trans. Instrum. Meas.* **69** 1505–18
[26] Pinnegar C R and Mansinha L 2013 The S-transform with windows of arbitrary and varying shape G *ASTM Geophysics* **68** 385–5
[27] Stockwell R G, Mansinha L and Lowe R P 1996 Localization of the complex spectrum: the S transform *IEEE Trans. Signal Process* **44** 998–1001
[28] Daubechies I, Lu J and Wu H T 2011 Synchrosqueezed wavelet transforms: an empirical mode decomposition-like tool *Appl. Comput. Harmon. Anal.* **30** 243–61
[29] Thakur G, Brevdo E, Fučkar N S and Wu H T 2013 The synchrosqueezing algorithm for time-varying spectral analysis: robustness properties and new paleoclimate applications *Signal Process.* **93** 1079–94
[30] Yi C C, Lv Y, Xiao H, Huang T and You G H 2018 Multisensor signal denoising based on matching synchrosqueezing wavelet transform for mechanical fault condition assessment *Meas. Sci. Technol.* **29** 244–58
[31] He D, Cao H R, Wang S B and Chen X F 2019 Time-reassigned synchrosqueezing transform: the algorithm and its applications in mechanical signal processing *Mech. Syst. Signal Process.* **117** 255–79
[32] Fourer D, Auger F, Czarnecki K, Meignen S and Flandrin P 2017 Chirp rate and instantaneous frequency estimation: application to recursive vertical synchrosqueezing *IEEE Signal Process Lett.* **24** 1724–8
[33] Jiang Q T and Suter B W 2017 Instantaneous frequencyestimation based on synchrosqueezing wavelet transform *Signal Process.* **138** 167–81
[34] Yu G, Lin T R, Wang Z H and Li Y Y 2020 Time-reassigned multisynchrosqueezing transform for bearing fault diagnosis of rotating machinery *IEEE Trans. Ind. Electron.* 10.1109/TIE.2020.2970571
[35] Wang S B, Chen X F, Cai G G, Chen B Q, Li X and He Z J 2014 Matching demodulation transform and synchrosqueezing in time–frequency analysis *IEEE Trans. Signal Process* **62** 69–84
[36] Yu K, Ma H, Han H Z, Zeng J, Li H F, Li X, Xu Z T and Wen B C 2019 Second order multi-synchrosqueezing transform for rub-impact detection of rotor systems *Mech. Mach. Theory* **140** 31–49
[37] Qu H Y, Li T T and Chen G D 2019 Synchro-squeezed adaptive wavelet transform *Mech. Syst. Signal Process.* **114** 366–77
[38] Behera R, Meignen S and Oberlin T 2018 Theoretical analysis of the second synchrosqueezing transform *Appl. Comput. Harmon. Anal.* **45** 379–404
[39] Wang S B, Chen X F, Tong C W and Zhao Z B 2017 Matching synchrosqueezing wavelet transform and application to aeroengine vibration monitoring *IEEE Trans. Instrum. Meas.* **66** 360–72
[40] Chen P, Wang K S, Zuo M J and Wei D D 2019 An ameliorated sychroeextracting transform based on upgraded local instantaneous frequency approxmation *Measurement* **148** 10693
[41] van Maanen H R E and Oldenziel A 1998 Estimation of turbulence power spectra from randomly sampled data by curve-fit to the autocorrelation function applied to laser-Doppler anemometry *Meas. Sci. Technol.* **9** 458–67
[42] Sun Z Q and Zhang H J 2007 Neural networks approach for prediction of gas–liquid two-phase flow pattern based on frequency domain analysis of vortex flowmeter signals *Meas. Sci. Technol.* **19** 015401
[43] Ding K Y, Xiao L F and Weng G R 2017 Impulsive noise detection by second-order differential image and noise removal using adaptive nearest neighbourhood filter *Signal Process.* **134** 224–33
[44] Baraniuk R, Flandrin P, Janssen A and Michel O 2001 Measuring time–frequency information content using the Renyi entropy *IEEE Trans. Inf. Theory* **47** 1391–409
[45] Kaiser J F 1974 Nonrecursive digital filter design using the I0-sinh window function *Proc. IEEE Int. Symp. Circuits and Systems* pp 20–3
[46] Oppenheim A V, Ronald W S and John R B 1999 *Discrete-Time Signal Processing* (Upper Saddle River, NJ: Prentice Hall) pp 474